Diameter Dependent Electron Transfer Kinetics in Semiconductor—Enzyme Complexes

Katherine A. Brown,[†] Qing Song,[‡] David W. Mulder,[†] and Paul W. King[*,†]

[†]Biosciences Center, National Renewable Energy Laboratory, Golden, Colorado 80401, United States, and [‡]IBM Almaden Research Center, San Jose, California 95120, United States

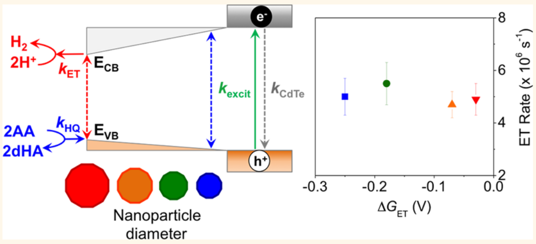

ABSTRACT Excited state electron transfer (ET) is a fundamental step for the catalytic conversion of solar energy into chemical energy. To understand the properties controlling ET between photoexcited nanoparticles and catalysts, the ET kinetics were measured for solution-phase complexes of CdTe quantum dots and *Clostridium acetobutylicum* [FeFe]-hydrogenase I (CaI) using time-resolved photoluminescence spectroscopy. Over a 2.0—3.5 nm diameter range of CdTe nanoparticles, the observed ET rate (k_{ET}) was sensitive to CaI concentration. To account for diameter effects on CaI binding, a Langmuir isotherm and two geometric binding models were created to estimate maximal CaI affinities and coverages at saturating concentrations. Normalizing the ET kinetics to CaI surface coverage for each CdTe diameter led to k_{ET} values that were insensitive to diameter, despite a decrease in the free energy for photoexcited ET (ΔG_{ET}) with increasing diameter. The turnover frequency (TOF) of CaI in CdTe—CaI complexes was measured at several molar ratios. Normalization for diameter-dependent changes in CaI coverage showed an increase in TOF with diameter. These results suggest that k_{ET} and H$_2$ production for CdTe—CaI complexes are not strictly controlled by ΔG_{ET} and that other factors must be considered.

KEYWORDS: nanoparticle · biohybrid · binding complex · interfacial electron-transfer · photochemical · hydrogen

Capture and conversion of solar energy for the clean and renewable production of fuels requires developing efficient and robust photochemical systems.[1,2] However, photocatalytic systems for H_2 production or CO_2 reduction from water splitting still present significant challenges toward understanding how to achieve optimal efficiencies.[3] Semiconductor nanoparticles have received considerable attention as building blocks for solar-to-fuel applications due to unique optical and physical properties.[4,5] At sizes below the Bohr radius (*e.g.*, nanoscale), semiconducting materials exhibit quantum confinement, which leads to size-dependent control of electronic properties.[6,7] Sophisticated fabrication methods can be used to control nanomaterial architectures and tune properties for use in solar energy conversion applications, including photocatalysis.[8] The integration of semiconductor nanoparticles with heterogeneous and homogeneous catalysts has led to a variety of photocatalytic systems for fuel production. Base and noble metal catalysts,[9−14] enzymes,[15−19] and synthetic compounds[20−23] have all been shown to participate in electron transfer (ET) with nanoparticles to generate H_2 under illumination.

We have demonstrated several systems for solar H_2 production utilizing chalcogenide nanoparticles coupled to *Clostridium acetobutylicum* [FeFe]-hydrogenase (CaI).[15,16] These systems show both high rates and quantum efficiencies of H_2 production. Recently, we measured the interfacial ET rate (k_{ET}) in complexes of CdS nanorods and CaI.[19] The value of interfacial k_{ET} was found to be comparable to the relaxation rate of the CdS nanorods. We hypothesized that the H_2 production rates and quantum yields may be controlled by the competition between ET and recombination pathways in these complexes. To further investigate how nanoparticle properties affect ET rates and H_2 production in semiconductor nanoparticle enzyme complexes, we explored the effect of nanoparticle diameter on the behavior of CdTe—CaI complexes. As nanoparticle diameter decreases, the band gap energy increases, resulting in a blue-shift of the absorbance peak and a more energetic conduction band electron. Decreasing the

* Address correspondence to paul.king@nrel.gov.

Received for review August 14, 2014 and accepted September 22, 2014.

10.1021/nn504561v

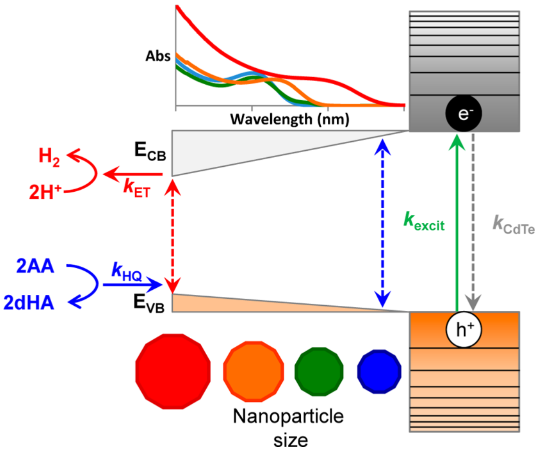

Figure 1. Energy level diagram showing the diameter dependent processes in CdTe–CaI photocatalysis (abbreviations: k_{ET}, rate constant for ET from CdS to CaI; k_{HQ}, rate constant for hole-quenching by ascorbate; AA, ascorbic acid; dHA, dehydroascorbate; k_{excit}, rate of exciton formation under illumination; k_{CdTe}, rate of excited state decay in CdTe, including both radiative and nonradiative pathways (*e.g.*, electron–hole recombination, carrier trapping)).

nanoparticle diameter also results in shorter excited state lifetimes, and faster recombination.[24] Thus, smaller nanoparticles have a larger ΔG_{ET} for interfacial ET (Figure 1), but a faster overall relaxation rate (k_{CdTe}). These two properties contribute to competing effects on the ET kinetics and H_2 production of CdTe–CaI complexes.[15,19] Changes in nanoparticle diameter will also alter the available binding sites due to changes in surface area and curvature, which can affect the binding affinity.[25,26] Each of these diameter-dependent properties contributes to the overall ET kinetics and photocatalytic rates of the complexes, and must be deconvoluted to understand the control of energy conversion at the nanoscale.

Here we report the effect of CdTe diameter on the behavior of CdTe–CaI complexes. Time resolved photoluminescence (TRPL) of CdTe–CaI complexes was measured over a range of CaI concentrations for each CdTe diameter, and used to determine the k_{ET} dependence on diameter. To correctly interpret the interfacial ET rate data from TRPL, two geometric binding models were developed to evaluate the dependence of CaI surface coverage on changes in CdTe diameter. Normalization of observed ET rates to the maximal number of CaI binding sites resulted in k_{ET} values that were constant over the CdTe diameter range, despite a decline in ΔG_{ET} with increasing diameter. We conclude that ET in CdTe–CaI is chemically coupled or gated, and is not strictly controlled by the free energy of the electron exchange (ΔG_{ET}). In the case of photocatalytic H_2 production, the turnover frequencies (TOF) increased with nanoparticle diameter (decreasing ΔG_{ET}). These results indicate that the H_2 production efficiency in CdTe–CaI complexes is controlled by a complex interplay of binding interactions, photogenerated reaction rates, and competition with internal relaxation pathways, which are sensitive to changes in nanoparticle diameter.

RESULTS AND DISCUSSION

CdTe–CaI Photoluminescence Lifetimes. The photocatalytic production of H_2 by CdTe–CaI complexes results from interfacial ET under illumination. The ET, in turn, affects the electron–hole recombination and photoluminescence (PL) properties of CdTe. Thus, the effect of CaI on relaxation of photoexcited CdTe can be probed by comparing the fluorescent lifetimes of CdTe either alone or in a complex with CaI. Four CdTe diameters were investigated, with diameter values of 2.0, 2.2, 2.8, and 3.5 nm determined from the first excited state 1S3/2(h) → 1S(e) transition peak wavelength as described in Yu *et al.*[27] Figure 2a shows an example of the fluorescence decay curves for 3.5 nm CdTe in the presence of CaI at CaI:CdTe molar ratios ranging from 0:1 to 10:1. Samples were excited with a 450 nm laser pulse, which populates high-energy states; however, relaxation of hot carriers occurs at ultrafast time scales (<1 ps).[28,29] Thus, we assume that electrons originate from the conduction band 1S(e).

As observed in Figure 2b, all four CdTe diameters showed decreased fluorescence lifetimes in the presence of CaI, where higher CaI:CdTe molar ratios led to gradually shorter lifetimes. We attribute this decrease to the addition of an ET pathway from CdTe to CaI (Figure 1), which results in faster exciton decay and shorter fluorescence lifetimes. The fluorescence decays were fit to triple exponential kinetic function, which provided the best quality fit as determined by chi-squared analysis (Supporting Information Table S1). The average fluorescent (PL) lifetime (τ_{obs}) for each CdTe diameter decreased with increasing CaI, reaching a plateau at high CaI:CdTe molar ratios (Supporting Information Table S2). This effect is due to the shift in the distribution of CdTe–CaI complexes toward maximal occupation of CdTe surface binding sites. At high CaI:CdTe molar ratios, all available surface binding sites on CdTe are occupied by CaI and the contribution of the CdTe → CaI interfacial ET pathway to the average lifetimes of photoexcited CdTe (τ_{obs}, Figure 2b) reaches a maximum.

To accurately evaluate the effect of CaI on CdTe photoluminescence, we derived an expression for τ_{obs} as a function of CaI concentration (Figure 2c). It has been shown for small molecule adsorbates on semiconductor nanoparticles that the fractional surface coverage (θ_{NP}) of the adsorbate (*i.e.*, CaI) can be calculated from the steady-state PL intensity changes of the nanoparticle (*i.e.*, CdTe):[30,31]

$$\theta_{NP} = \frac{PL_\theta - PL_0}{PL_s - PL_0} \quad (1)$$

where PL_θ is the PL intensity at a given adsorbate concentration, and PL_S and PL_0 are the PL intensities for CdTe at saturating and zero (bare nanoparticle) coverages, respectively. Here we extend this analysis to

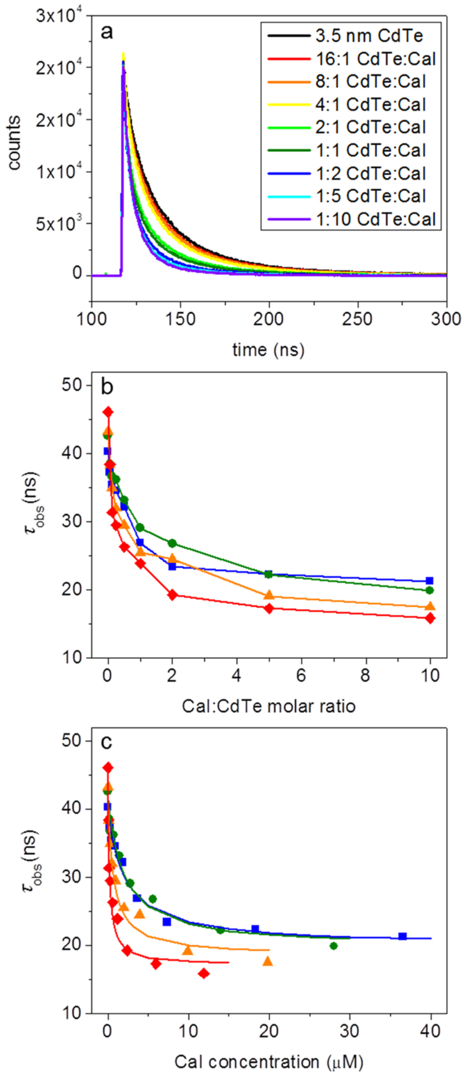

Figure 2. CdTe−Cal complex lifetime. (a) Time resolved photoluminescence emission decay of 3.5 nm CdTe in complex with Cal at Cal:CdTe molar ratios from 0:1 to 10:1 (1.2 μM CdTe). (b) Average fluorescent lifetimes for 2.0 nm (blue squares), 2.2 nm (green circles), 2.8 nm (orange triangles), and 3.5 nm (red diamonds) CdTe, for each Cal: CdTe molar ratio from 0:1 to 10:1. (c) Average fluorescent lifetimes for 2.0 nm (blue squares), 2.2 nm (green circles), 2.8 nm (orange triangles), and 3.5 nm (red diamonds) CdTe as a function of Cal concentration (CdTe concentration for each diameter adjusted to yield A_{450} = 0.05). Fits of eq 8 for each data set are shown as solids lines.

evaluate the effect of Cal adsorption on CdTe nanoparticle PL. Cal adsorption differs from small molecule behavior in the total number of interactions (Cal < small molecule), and in conformational states of molecular complexes. The measured effect of adsorbed Cal on CdTe PL is an average for an ensemble of different CdTe−Cal conformational complexes, and will still be proportional to the fractional surface coverage, θ_{NP}. We can use eq 2 to relate PL$_\theta$ to τ_{obs} measured in TRPL experiments:[32]

$$\mathrm{PL}_\theta \propto \Phi_\theta = \frac{\tau_{obs}}{\tau_{RR}} \qquad (2)$$

TABLE 1. Calculated Values of CdTe−Cal Fluorescent Lifetime, Equilibrium Constant, and Free-Energy of Adsorption

CdTe diameter (nm)	K_{EQ} (μM^{-1})^a	ΔG_{ABS} (kcal mol^{-1})	τ_s (ns)^a
2.0	0.5 ± 0.1	7.7 ± 0.3	20.0 ± 1.3
2.2	0.7 ± 0.2	7.9 ± 0.4	19.6 ± 1.4
2.8	1.3 ± 0.3	8.3 ± 0.2	17.8 ± 1.2
3.5	4.2 ± 0.9	9.0 ± 0.3	16.4 ± 1.2

[a] Calculated from fits of τ_{obs} *vs* [Cal] with eq 8.

where Φ_θ is the PL quantum yield (PLQY) of CdTe at a given Cal concentration, and τ_{RR} is the radiative lifetime of a bare CdTe. The τ_{RR} can be calculated from the average PL lifetime (τ_{NP}) and PLQY of the bare CdTe (Φ_0), as shown in eq 3.

$$\Phi_0 = \frac{\tau_{NP}}{\tau_{RR}} \qquad (3)$$

The PLQY for a given Cal concentration then becomes

$$\Phi_\theta = \frac{\tau_{obs}\Phi_0}{\tau_{NP}} \qquad (4)$$

$$\Phi_S = \frac{\tau_S\Phi_0}{\tau_{NP}} \qquad (5)$$

where τ_s and Φ_s are the PL lifetime and PLQY, respectively, of CdTe at saturating Cal coverages. The fractional surface coverage, θ_{NP} can be expressed as a function of fluorescence lifetimes (eq 6).

$$\theta_{NP} = \frac{\tau_{obs} - \tau_{NP}}{\tau_S - \tau_{NP}} \qquad (6)$$

The Langmuir isotherm defines θ for CdTe−Cal complexes as a function of Cal concentration and the equilibrium binding constant for CdTe + Cal ↔ CdTe−Cal (eq 7).

$$\theta_{CdTe} = \frac{K_{EQ}[\mathrm{Cal}]}{1 + K_{EQ}[\mathrm{Cal}]} \qquad (7)$$

Combining eqs 6 and 7 leads to an expression for τ_{obs} as a function of τ_{NP}, τ_S and K_{EQ}.

$$\tau_{obs} = \tau_{NP} + \frac{K_{EQ}[\mathrm{Cal}](\tau_S - \tau_{NP})}{1 + K_{EQ}[\mathrm{Cal}]} \qquad (8)$$

Equation 8 was used to analyze the effect of Cal concentration on the fluorescent lifetime for each diameter, and extrapolate the CdTe lifetime at saturated Cal surface binding. The solid lines in Figure 2c show fits of τ_{obs} *vs* Cal concentration (symbols) using eq 8. The calculated values of τ_s and K_{EQ} for each CdTe diameter are listed in Table 1.

Cal Binding Equilibria. The value of K_{EQ} derived from eq 8 allows us to determine the Cal binding affinity for CdTe, ΔG_{ABS}, and how this value changes with diameter. Each value of ΔG_{ABS} for Cal binding to CdTe was determined from $\Delta G_{ABS} = RT \ln K_{EQ}$. As shown in

Table 1, there is a small increase in ΔG_{ABS} with increasing CdTe diameter, but all values are within the range of electrostatic chemisorption previously described for MPA–capped nanoparticle–CaI interactions.[15,16] The slight increase in ΔG_{ABS} is possibly a result of the larger surface area, and thus the number of CaI binding sites, with increasing nanoparticle diameter.[33] The diameter-dependent K_{EQ} values were also used to calculate the concentrations of CdTe–CaI complexes in solution. For each molar ratio, the equilibrium concentrations of CdTe–CaI were similar across the CdTe diameter range (Supporting Information Table S3), meaning that the contribution of CdTe–CaI complexes to the average lifetime for any given molar ratio are similar.

Surface Binding Models for CdTe–CaI Complexes. We hypothesize that the observed trend in ΔG_{ABS} with diameter for CdTe–CaI is the result of the effect of nanoparticle diameter on CaI binding capacity. Changes in nanoparticle surface area and curvature alters the number of surface binding sites, which has been shown to alter binding densities of nm-sized molecules.[10,25,33,34]

To normalize for this effect of increasing CdTe diameter on CaI surface binding, we developed geometric models of the CaI binding to the surface of CdTe. We have previously modeled CdS nanorod–CaI complex distribution in solution based on a Poisson distribution.[16,19] When the number of CaI approaches the total binding capacity, the Poisson distribution predicts some surface coverages will exceed the maximum binding capacity. The effect was accounted for by limiting the ET measurements on CdS nanorod–CaI complexes to molar ratios that were lower than the CdS surface-binding limit for CaI. However, in the CdTe–CaI system, the nanoparticles and CaI are in a similar size regime, limiting the surface binding capacity and making a Poisson distribution analysis impractical.

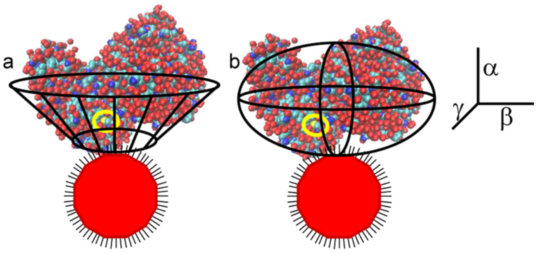

Figure 3. Geometric models (to scale) of CaI binding on 3.5 nm CdTe: (a) cone model; (b) ellipsoid model.

TABLE 2. CaI Binding Sites for Each Diameter CdTe

	CaI binding sites	
CdTe diameter (nm)	cone model	ellipsoid model
2.0	3	5
2.2	3	5
2.8	4	7
3.5	5	8

Here, we developed two complementary geometric models to calculate the maximum surface coverage of CaI for each CdTe diameter (details in Supporting Information). Both models rely on the X-ray crystal structure of [FeFe]-hydrogenase I from *Clostridium pasteurianum* (CpI, PDB code 1feh),[35] which has 70% sequence identity with CaI,[36,37] to define the dimensions of CaI. Additionally, we assume the nanoparticle to be a perfect sphere with a radius that includes the length of the MPA ligand (~5 Å). In the cone model, CaI was represented as a truncated elliptical cone (Figure 3a), where the X-ray structure of CpI[35] was used to determine dimensions of the elliptical boundaries of the cone. The maximum length dimensions of CpI were used to set the upper bound, whereas the lower bound ellipse dimension was based on the surface area at the distal [4Fe–4S] cluster (Figure 3a, yellow circle). This cluster is predicted to be the site of *in vivo* ET from ferredoxin (Fd) into CpI/CaI,[35,36] and the adjacent surface is the proposed CdTe binding site.[15,16] The “footprint” of the CaI binding site for each CdTe diameter was calculated from the angles of deflection of the long and short dimensions of the elliptical cone with the center of the nanoparticle (details in Supporting Information). The maximum CaI coverage for each diameter was calculated from the resulting elliptical footprint and the surface area of the nanoparticle. The angle of deflection is directly related to the radius of curvature of the nanoparticle, so the elliptical footprints vary with CdTe diameter. This results in a smaller relative CaI footprint on larger diameter, lower curvature nanoparticles. The maximum CaI coverages for each CdTe diameter are listed in Table 2.

For the ellipsoid-binding model, CaI was modeled as an enclosed ellipse (Figure 3b) with the axes defined by the maximal length and width dimensions of the CpI X-ray structure. For each CdTe diameter, we defined a binding sphere with a radius $R = r + 2\alpha$, around the nanoparticle, where r is the nanoparticle radius and α is the vertical dimension of CaI shown in Figure 3b. The volume available for CaI binding (V_B) was defined by eq 9.

$$V_B = \frac{4}{3}\pi[(r+2\alpha)^3 - r^3] \qquad (9)$$

The maximum CaI binding coverage was calculated from the CaI ellipsoid volume and V_B (Table 2).

Both binding models show similar trends for the effect of CdTe diameter on CaI coverage. In both, larger diameter particles have higher binding capacities, as expected; however, this increase in maximum coverage is considerably smaller than the corresponding increase in nanoparticle surface area. The ratio of the surface areas of the largest and smallest diameter CdTe is 2.25, whereas both binding models predict that the ratio of corresponding CaI binding capacities is ~1.6. Nanoparticle binding capacities for large molecules like CaI can differ significantly from those predicted

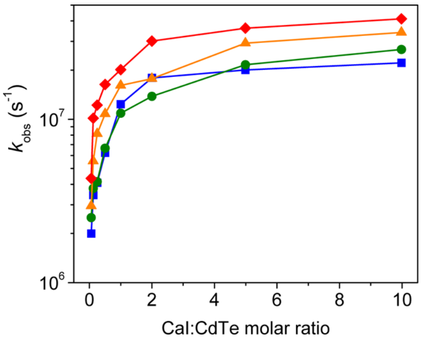

Figure 4. Electron transfer rates in CdTe–Cal complexes. k_{obs} values calculated from eq 10 for 2.0 nm (blue squares), 2.2 nm (green circles), 2.8 nm (orange triangles), and 3.5 nm (red diamonds) CdTe, for each Cal:CdTe molar ratio from 0:1 to 10:1.

by simple surface area calculations.[38] This illustrates the importance of nanoparticle curvature on biomolecular coverage in systems where the components are similar length-scales. Binding capacities, together with experimental measurements of binding affinities, must all be used to estimate surface coverage for each diameter of CdTe. This is critical to evaluating ET kinetics from optical spectroscopy measurements, which exhibit a strong dependence on binding stoichiometries.[33,34]

Electron Transfer Kinetics. As noted above, the observed decrease in CdTe lifetime with increasing Cal concentration is attributed to the addition of a photo-driven ET pathway from CdTe → Cal. The change in fluorescent lifetime can be used to calculate the rate of electron transfer (k_{obs}) using eq 10:

$$k_{obs} = \frac{1}{\tau_{obs}} - \frac{1}{\tau_{NP}} \qquad (10)$$

where k_{obs} measures the average ET rate at a specific Cal:CdTe molar ratio. Figure 4 shows the k_{obs} values for each CdTe diameter plotted against increasing Cal:CdTe molar ratios. The values of k_{obs} increases with Cal concentration due to the increase in Cal surface coverage at higher Cal:CdTe, which increases the probability of an ET event. The increase in k_{obs} is linear when the Cal:CdTe molar ratio is low compared to saturation, consistent with previous CdS–Cal ET rate measurements.[19] At saturating levels of Cal, the average ET rate can be estimated from CdTe fluorescent lifetime at Cal saturation, τ_s (Table 1) in place of τ_{obs} in eq 10. This k_s value for each diameter is listed in Table 3.

Since the ET kinetics are sensitive to the Cal concentration, a higher number of Cal molecules are bound to the larger diameter CdTe at saturation, resulting in higher k_s values. To account for this effect, we use the Cal binding models to normalize the ET kinetics per Cal bound using eq 11:

$$k_{ET} = k_s/N \qquad (11)$$

where N is the total number of Cal binding sites for each CdTe diameter (Table 2) and k_{ET} is the intrinsic rate for ET between CdTe → Cal.

TABLE 3. Electron Transfer Kinetics for CdTe–Cal Complexes

CdTe diameter (nm)	k_s ($\times$ 10^7 Cal s^{-1})[a]	k_{ET} ($\times$ 10^6 s^{-1})[b] cone model	ellipsoid model
2.0	2.5 ± 0.3	8.4 ± 1.1	5.0 ± 0.7
2.2	2.8 ± 0.4	9.2 ± 1.3	5.5 ± 0.8
2.8	3.3 ± 0.4	8.2 ± 0.9	4.7 ± 0.5
3.5	3.9 ± 0.5	7.8 ± 0.9	4.9 ± 0.6

[a] Calculated from τ_s values using eq 10. [b] k_{ET} calculated from k_s using eq 11.

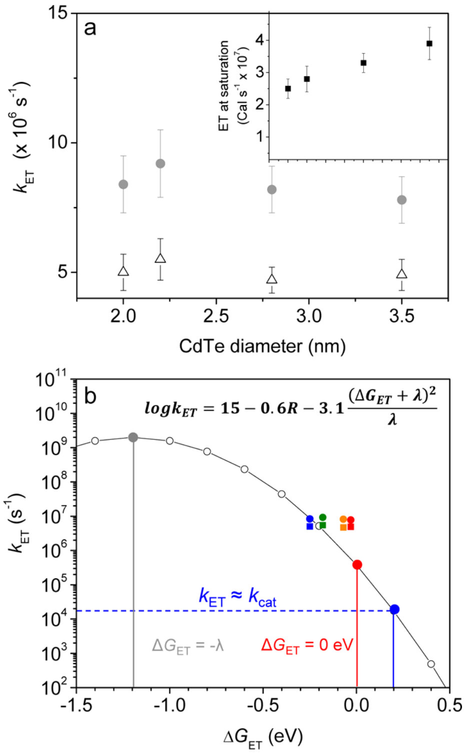

Figure 5. Normalized ET kinetics. (a) k_{ET} normalized to maximal Cal coverages predicted by the cone (gray circles) and ellipsoid (white triangles) models (inset, ET rate at Cal saturation (k_S) for 2.0, 2.2, 2.8, and 3.5 nm CdTe). (b) Log plot of CdTe–Cal k_{ET} values normalized for cone (circles) and ellipsoid (squares) models and predicted biological ET kinetics (equation shown) *vs* ΔG_{ET} values from Supporting Information Table S4.

The normalized k_{ET} values for each diameter are listed in Table 3. Regardless of which model was used, the resulting k_{ET} values were found to be similar across the diameter range (Figure 5a). This trend is despite the fact that the value of ΔG_{ET} increased with decreasing diameter (Supporting Information Table S4). These results illustrate the importance of modeling nanoparticle surface coverage for measuring ET kinetics. Changes in nanoparticle diameter can result in significant changes to the binding behavior of electron acceptors, and accurate analysis of ET requires accurate estimates of surface coverage. The trend for CdTe–Cal contrasts with previous measurements of ET kinetics between semiconductor nanoparticles and molecular complexes, where k_{ET} was observed to increase with decreasing nanoparticle diameter.[39−42]

The observed trend in k_{ET} differs from Marcus theory based predictions of protein ET as a function of ΔG_{ET}. Figure 5b shows the predicted values of k_{ET} for CdTe → Cal over a range of ΔG_{ET} using the Page-Moser-Dutton empirical formula for protein ET.[43] We assume an ET reorganization energy of 1.2 eV for [4Fe−4S] clusters,[43,44] with minimal contribution from the CdTe.[42,45] An ET distance from the nanoparticle surface to the distal [4Fe−4S] cluster of 9.5 Å was derived from a static binding model and based on the average distance between the MPA carboxyl group and the Cal distal [4Fe−4S] cluster.[15] This analysis predicts a gradually decreasing k_{ET} for $\Delta G_{ET} < 1.2$ eV, which corresponds to the range of ΔG_{ET} values for ET between CdTe and Cal. These ΔG_{ET} values were measured from pH-dependent methyl viologen reduction assays (Supporting Information Figures S2 and S3 and Table S4) as previously described.[15,16] The normalized k_{ET} values obtained from eq 11 using the cone (circles) and ellipsoid (squares) binding models are shown in Figure 5b. Overall, the k_{ET} values are reasonably predicted by the model, but the trend of k_{ET} *vs* free-energy of ET differs from that predicted by Marcus theory or the Page-Moser-Dutton formulation.

The apparent insensitivity of k_{ET} to changes in CdTe diameter indicates that the ET step from CdTe to the Cal distal [4Fe−4S] cluster might be coupled to a chemical step, or is gated. One possibility is that 1e$^-$ reduction of the distal [4Fe−4S] cluster proceeds *via* protonation, *e.g.*, proton-coupled electron transfer (PCET). Cal is structurally homologous to CpI,[35,37] and the X-ray structure of CpI shows coordination of the distal [4Fe−4S] cluster is site-differentiated, having 3 cysteine (Cys) and 1 histidine (His) ligands. Similar site-differentiated FeS clusters exist in other redox proteins, notably Rieske clusters,[46] mitoNEET,[47,48] nitrate reductase,[49] and [NiFe]-hydrogenase.[50] Exchange of His → Cys in FeS cluster ligation effected enzyme activity, interfacial ET rate, FeS cluster E_m, or PCET, confirming the significance of His-ligation on tuning FeS cluster potentials and rates of intermolecular ET exchange in these proteins. Depending on the nature of proton-coupled reduction of the His-ligated Cal distal [4Fe−4S] cluster, the weak effect of ΔG_{ET} on CdTe → Cal k_{ET} is consistent with PCET-based interfacial ET.[51−53] A PCET mechanism would also explain the discrepancy between our results and previous measurements of ET kinetics between semiconductor nanoparticles and molecular or nanoparticle electron acceptors.[39−42] In these systems, k_{ET} is consistent with ΔG_{ET} dominated ET kinetics.

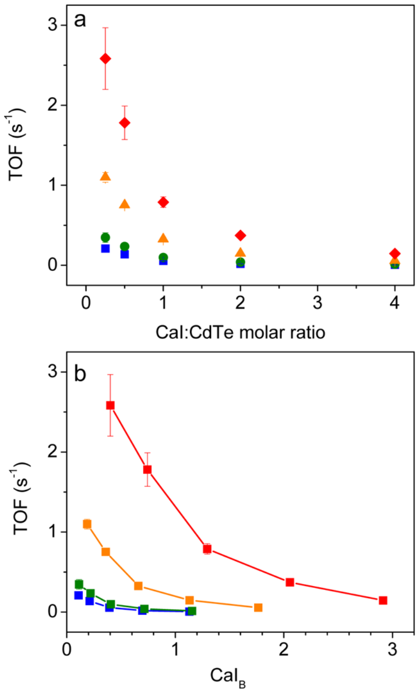

Figure 6. Cal TOF in CdTe−Cal complexes. a) TOF at 1:4, 1:2, 1:1, 2:1, and 4:1 Cal:CdTe molar ratios for 2.0 nm (blue squares), 2.2 nm (green circles), 2.8 nm (orange triangles), and 3.5 nm (red diamonds) CdTe. b) TOF at 1:4, 1:2, 1:1, 2:1, and 4:1 Cal:CdTe molar ratios as a function the average Cal bound per CdTe (Cal$_B$). Samples illuminated for 5 min with 405 nm light (2500 μmol photon m^{-2} s^{-1}) with 100 mM AA. CdTe concentration normalized to A_{405} = 0.01 ([CdTe] 2.0 nm, 0.31 μM; 2.2 nm, 0.28 μM; 2.8 nm, 0.13 μM; and 3.5 nm, 0.073 μM).

Analysis of CdTe Diameter Effect on H_2 Production. Previous results with both CdS−Cal and CdTe−Cal complexes have shown that low Cal:CdTe ratios show the highest values for TOF (mol^{-1} H_2 mol^{-1} Cal s^{-1}).[15,16] We measured the effect of molar ratio here to determine whether CdTe diameter influenced this trend (Figure 6a). The result was consistent with previous observations: the low Cal:CdTe ratios showed maximal TOF. The trend in Figure 6a shows that TOF also increases with CdTe diameter for each Cal:CdTe molar ratio, as did H_2 yields (Supporting Information Figure S4). Since the number of Cal binding sites (N) per CdTe increases with diameter (Table 3) the distribution of complexes (*i.e.*, fraction of CdTe−Cal with 1, 2, 3, *etc.* Cal bound) at each Cal:CdTe molar ratio differs for each diameter. Thus, the effect of CdTe diameter on TOF at a specific molar ratio may be the result of the change in the distribution of CdTe−Cal complexes. To account for this effect, the fractional surface coverage θ_{CdTe} for each Cal:CdTe molar ratio was calculated using eq 7 and the K_{EQ} values listed in Table 1. Using the θ_{CdTe} values together with the values for N determined by the two binding models, the average Cal bound per CdTe (Cal$_B$) was calculated using eq 12.

$$\mathrm{Cal_B} = N\theta_{CdTe} \qquad (12)$$

Figure 6b is a plot of the TOF values *vs* Cal$_B$ for each CdTe diameter based on the cone binding model (TOF *vs* Cal$_B$ for the ellipsoid model is shown in Supporting Information Figure S8).

Two trends are observed in Figure 6b. First, the TOF of all diameter complexes increases as CaI_B shifts to lower values. Again this is consistent with TOF and H_2 quantum yields being highest for mixtures that favor a high fraction of CdTe−CaI complexes with only 1 CaI bound.[16] Due to photon-limiting conditions (average absorbed photon flux ≈34 photons $CdTe^{-1}$ s^{-1}, ≈0.34% of CaI TOF[54]) there is competition for photoexcited electrons among multiple CaI molecules on a single CdTe. Because H_2 production is a two-electron process, a high CaI coverage results in lower H_2 production TOF and quantum yields. This effect was demonstrated in CdS-CaI complexes, where increasing the CaI:CdS molar ratio effectively decreased the quantum efficiency of electron transfer per CaI due to increased coverage and competition for electrons.[19] The second trend evident in Figure 6b is the increase in TOF, and H_2 quantum yields (also summarized in Supporting Information Figure S4, Table S5) with CdTe diameter for each CaI_B value. The analysis differs from Figure 6a by normalizing for increasing *N* with diameter.

These diameter-dependent trends differ from previous reports of nanoparticle-based H_2 production,[10,55] where decreasing nanoparticle diameter resulted in production of higher amounts of H_2. In those systems, the trend is attributed to the corresponding increase in ΔG_{ET} for a surface-state catalyzed proton reduction reaction with decreasing CdSe diameter. In contrast, for CdTe−CaI complexes the difference in ΔG_{ET} does not significantly affect k_{ET} or the photocatalytic rates. Rather, as we observed previously the intrinsic nanoparticle recombination processes in both CdS−CaI and CdTe−CaI complexes directly compete with ET.[15,19] This effect accounts for the rise in TOF with increasing CdTe diameter, since the corresponding photoluminescent lifetimes (τ_{NP}, Supporting Information Table S2) increase, whereas k_{ET} remains essentially constant at $\sim 10^7$ s^{-1}. In other words, the CdTe → CaI ET step is unaffected by changes in ΔG_{ET}, which leads to charge recombination control of the H_2 production kinetics and efficiencies.

CONCLUSIONS

In summary, we have investigated the effect of CdTe diameter on the interfacial ET kinetics, surface binding capacity and photocatalytic H_2 production of CdTe−CaI complexes. When diameter dependent changes in surface bound CaI are taken into account, both the k_{ET} and the TOF for CdTe−CaI show surprising trends. Despite a decrease in ΔG_{ET} with increasing CdTe diameter, the CdTe → CaI k_{ET} values are constant across the diameter range investigated, while TOF increases with increasing diameter. Both these trends contrast with previous reports of semiconductor nanoparticle ET and H_2 production systems. We attribute this difference mainly to the site-differentiated [4Fe−4S] cluster of CaI, which effectively minimizes the influence of ΔG_{ET} on the CdTe → CaI ET kinetics. The implication is that incorporation of proton-transfer controlled ET relays similar to the distal [4Fe−4S] cluster of CaI as components of synthetic catalysts might prove beneficial to leveling interfacial k_{ET} and driving photochemical reactions over a broader potential range.

The flat, ΔG_{ET} independent k_{ET} reveals that in CdTe−CaI complexes, the CdTe recombination rates largely control H_2 photoproduction. As a consequence the use of wider band gap, large-diameter nanoparticles are possible, which both minimizes rates of competing reactions while improving quantum yields due to higher extinction coefficients and utilization of more of the solar spectrum. Generally, these results indicate that photocatalytic efficiencies of nanoparticle−catalyst complexes are a function of a complex interplay between interfacial ET and recombination processes, and that competition between individual catalysts significantly affects rates of multielectron reactions.

MATERIALS AND METHODS

[FeFe]-Hydrogenase Expression and Purification. The StrepII-tagged [FeFe]-hydrogenase I from *C. acetobutylicum* (CaI) was expressed and purified from *Escherichia coli* as previously described.[36] Specific activities of CaI preparations were measured as the H_2 evolved from sodium dithionite (Riedel-de Haen) reduced MV (5 mM, Sigma).[36] Purified CaI had specific activities of ∼1300 μmol H_2 mg^{-1} min^{-1}, with protein concentrations determined by the Bradford assay using Hemoglobin as the standard.

CdTe Nanoparticle Synthesis. All CdTe nanoparticles used in this study were produced by microwave-assisted synthesis. For example, in a typical synthesis of CdTe nanoparticles with a size of 2.8 nm, first 0.8 mmol of $CdCl_2$ (Sigma-Aldrich) was dissolved in 40 mL of water, and 1.92 mmol of 2-mercaptopropionic acid (MPA, Sigma-Aldrich) was added followed by the addition of 1 M NaOH solution to reach a pH 8.0−8.5. A freshly made NaHTe solution (total amount of Te was 0.4 mmol) was quickly injected into this $CdCl_2$−MPA solution under vigorously stirring at room temperature. After the reaction was kept for 5 min, 25 mL of this solution was transferred to an 80 mL vessel. The 80 mL vessel was loaded into a single mode microwave reactor (Discover CEM, Inc.). The microwave-assisted synthesis was carried out in a fixed power mode with 300 W power output at 100 °C for 30 min. All other sizes of CdTe nanoparticles were synthesized in a similar way. The size of CdTe nanoparticles was controlled by the reaction temperature and time. The CdTe concentrations were determined from the absorbance at the first excitonic transition peak wavelength, using the equations developed by Yu *et al.*[27] (2.0 nm, $\lambda = 490$ nm, $\varepsilon = 45\,620$ M^{-1} cm^{-1}; 2.2 nm, $\lambda = 495$ nm, $\varepsilon = 53\,395$ M^{-1} cm^{-1}; 2.8 nm, $\lambda = 520$ nm, $\varepsilon = 89\,600$ M^{-1} cm^{-1}; 3.4 nm, $\lambda = 568$ nm, $\varepsilon = 135\,300$ M^{-1} cm^{-1}).

TRPL Measurements. Samples of CdTe in Tris-HCl pH 7 buffer were prepared in sealed fluorescence cuvettes with a 3 × 5 mm window and a 3 mm path length. All samples were prepared such that the CdTe absorption at 450 nm = 0.05. For each CdTe diameter, CaI concentrations yielded 1:16, 1:8, 1:4, 1:2, 1:1, 2:1, 5:1, and 10:1 CaI:CdTe molar ratios. Samples were illuminated at

λ = 450 nm with a Fianium Supercontinuum laser. The PL emission was collected for each CdTe sample at the first excitonic transition peak (PL emission peak position: 2.0 nm λ_{em} = 531 nm; 2.2 nm, λ_{em} = 537 nm; 2.8 nm, λ_{em} = 566 nm; 3.4 nm, λ_{em} = 639 nm) (MicroHR photodetector, Horiba Scientific) and analyzed by a time-correlated single photon counting board (Horiba Scientific). The instrument response function for lifetime measurements had a full width at half-maximum of 0.75 ns.

Photochemical CdTe−CaI H_2 Production. Samples of CdTe−CaI containing 100 mM ascorbic acid (Fluka) in Tris-HCl pH 7 buffer were illuminated for 5 min with an Ocean Optics 405 nm LED light (750 mW, 500 mA, Ocean Optics) at 2500 μmol photon m^{-2} s^{-1} (LI-250 light meter, LI-COR Biosciences). All samples were prepared such that the absorbance at 405 nm had an OD = 0.01. For each CdTe diameter, CaI concentrations yielded 1:4, 1:2, 1:1, 2:1, and 4:1 CaI:CdTe molar ratios. Each sample was illuminated in 1.5 mL serum vials with an illuminated surface area of 5 mm^2. Headspace H_2 was measured after 5 min by GC (Agilent 7890A Gas Chromatograph; 5 Å mol sieve column (Supelco). H_2 production was only observed by CdTe−CaI complexes under illumination.

Conflict of Interest: The authors declare no competing financial interest.

Acknowledgment. K.A.B., D.W.M, and P.W.K. gratefully acknowledge funding support by the U.S. Department of Energy, Office of Science, Office of Basic Energy Sciences, Division of Chemical Sciences, Geosciences, and Biosciences; and support of the U.S. Department of Energy under Contract No. DE-AC36-08-GO28308 with the National Renewable Energy Laboratory. Q.S gratefully acknowledges insightful discussions with X. Ai, and research support from IBM for synthesis of CdTe nanoparticles. K.A.B acknowledges the assistance of A. Ferguson of the NREL Solar Photochemistry Group with TRPL measurements. All the authors gratefully acknowledge M. W. Ratzloff, G. Dukovic and M. Wilker for helpful and insightful discussions.

Supporting Information Available: CdTe Optical properties; CdTe and CdTe−CaI fluorescent lifetime calculations and fits; equilibrium CdTe−CaI complex concentration; CdTe Nanoparticle Reduction Potential protocol and results; CdTe potentials of ΔG_{ET} values; nmol H_2 produced by CdTe−CaI complexes; quantum yield of H_2 production for 1:2 CaI:CdTe; physical dimensions of [FeFe]-hydrogenase CaI; binding model details; CaI TOF in CdTe−CaI complexes normalized for ellipsoid model. This material is available free of charge *via* the Internet at http://pubs.acs.org.

REFERENCES AND NOTES

1. Gust, D.; Moore, T. A.; Moore, A. L. Solar Fuels *via* Artificial Photosynthesis. *Acc. Chem. Res.* **2009**, *42*, 1890–1898.
2. McKone, J. R.; Lewis, N. S.; Gray, H. B. Will Solar-Driven Water-Splitting Devices See the Light of Day? *Chem. Mater.* **2014**, *26*, 407–414.
3. Tran, P. D.; Wong, L. H.; Barber, J.; Loo, J. S. C. Recent Advances in Hybrid Photocatalysts for Solar Fuel Production. *Energy Environ. Sci.* **2012**, *5*, 5902–5918.
4. Kamat, P. V. Manipulation of Charge Transfer Across Semiconductor Interface. A Criterion That Cannot Be Ignored in Photocatalyst Design. *J. Phys. Chem. Lett.* **2012**, *3*, 663–672.
5. Wilker, M. B.; Schnitzenbaumer, K. J.; Dukovic, G. Recent Progress in Photocatalysis Mediated by Colloidal II-VI Nanocrystals. *Isr. J. Chem.* **2012**, *52*, 1002–1015.
6. Alivisatos, A. P. Semiconductor Clusters, Nanocrystals, and Quantum Dots. *Science* **1996**, *271*, 933–937.
7. Nozik, A. J.; Beard, M. C.; Luther, J. M.; Law, M.; Ellingson, R. J.; Johnson, J. C. Semiconductor Quantum Dots and Quantum Dot Arrays and Applications of Multiple Exciton Generation to Third-Generation Photovoltaic Solar Cells. *Chem. Rev.* **2010**, *110*, 6873–6890.
8. Banin, U.; Ben-Shahar, Y.; Vinokurov, K. Hybrid Semiconductor−Metal Nanoparticles: From Architecture to Function. *Chem. Mater.* **2014**, *26*, 97–110.
9. Amirav, L.; Alivisatos, A. P. Photocatalytic Hydrogen Production with Tunable Nanorod Heterostructures. *J. Phys. Chem. Lett.* **2010**, *1*, 1051–1054.
10. Gao, P.; Liu, J.; Lee, S.; Zhang, T.; Sun, D. D. High Quality Graphene Oxide-Cds-Pt Nanocomposites for Efficient Photocatalytic Hydrogen Evolution. *J. Mater. Chem.* **2012**, *22*, 2292–2298.
11. O'Connor, T.; Panov, M. S.; Mereshchenko, A.; Tarnovsky, A. N.; Lorek, R.; Perera, D.; Diederich, G.; Lambright, S.; Moroz, P.; Zamkov, M. The Effect of the Charge-Separating Interface on Exciton Dynamics in Photocatalytic Colloidal Heteronanocrystals. *ACS Nano* **2012**, *6*, 8156–8165.
12. Osterloh, F. E. Inorganic Materials as Catalysts for Photochemical Splitting of Water. *Chem. Mater.* **2007**, *20*, 35–54.
13. Yan, H.; Yang, J.; Ma, G.; Wu, G.; Zong, X.; Lei, Z.; Shi, J.; Li, C. Visible-Light-Driven Hydrogen Production with Extremely High Quantum Efficiency on Pt−PdS/CdS Photocatalyst. *J. Catal.* **2009**, *266*, 165–168.
14. Zhu, H.; Song, N.; Lv, H.; Hill, C. L.; Lian, T. Near Unity Quantum Yield of Light-Driven Redox Mediator Reduction and Efficient H_2 Generation Using Colloidal Nanorod Heterostructures. *J. Am. Chem. Soc.* **2012**, *134*, 11701–11708.
15. Brown, K. A.; Dayal, S.; Ai, X.; Rumbles, G.; King, P. W. Controlled Assembly of Hydrogenase-CdTe Nanocrystal Hybrids for Solar Hydrogen Production. *J. Am. Chem. Soc.* **2010**, *132*, 9672–9680.
16. Brown, K. A.; Wilker, M. B.; Boehm, M.; Dukovic, G.; King, P. W. Characterization of Photochemical Processes for H2 Production by CdS Nanorod−[FeFe] Hydrogenase Complexes. *J. Am. Chem. Soc.* **2012**, *134*, 5627–5636.
17. Reisner, E.; Powell, D. J.; Cavazza, C.; Fontecilla-Camps, J. C.; Armstrong, F. A. Visible Light-Driven H2 Production by Hydrogenases Attached to Dye-Sensitized TiO_2 Nanoparticles. *J. Am. Chem. Soc.* **2009**, *131*, 18457–18466.
18. Selvaggi, A.; Tosi, C.; Barberini, U.; Franchi, E.; Rodriguez, F.; Pedroni, P. *In Vitro* Hydrogen Photoproduction Using *Pyrococcus furiosus* Sulfhydrogenase and TiO_2. *J. Photochem. Photobiol., A* **1999**, *125*, 107–112.
19. Wilker, M. B.; Shinopoulos, K. E.; Brown, K. A.; Mulder, D. W.; King, P. W.; Dukovic, G. Electron Transfer Kinetics in CdS Nanorod−[FeFe]-Hydrogenase Complexes and Implications for Photochemical H_2 Generation. *J. Am. Chem. Soc.* **2014**, *136*, 4316–4324.
20. Artero, V.; Fontecave, M. Solar Fuels Generation and Molecular Systems: Is It Homogeneous or Heterogeneous Catalysis? *Chem. Soc. Rev.* **2013**, *42*, 2338–2356.
21. Kumar, B.; Beyler, M.; Kubiak, C. P.; Ott, S. Photoelectrochemical Hydrogen Generation by an [FeFe] Hydrogenase Active Site Mimic at a P-Type Silicon/Molecular Electrocatalyst Junction. *Chem.—Eur. J.* **2012**, *18*, 1295–1298.
22. Wang, F.; Wang, W.-G.; Wang, X.-J.; Wang, H.-Y.; Tung, C.-H.; Wu, L.-Z. A Highly Efficient Photocatalytic System for Hydrogen Production by a Robust Hydrogenase Mimic in an Aqueous Solution. *Angew. Chem., Int. Ed.* **2011**, *50*, 3193–3197.
23. Wen, F.; Li, C. Hybrid Artificial Photosynthetic Systems Comprising Semiconductors as Light Harvesters and Biomimetic Complexes as Molecular Cocatalysts. *Acc. Chem. Res.* **2013**, *46*, 2355–2364.
24. Bang, J. H.; Kamat, P. V. CdSe Quantum Dot−Fullerene Hybrid Nanocomposite for Solar Energy Conversion: Electron Transfer and Photoelectrochemistry. *ACS Nano* **2011**, *5*, 9421–9427.
25. Cederquist, K. B.; Keating, C. D. Curvature Effects in DNA:Au Nanoparticle Conjugates. *ACS Nano* **2009**, *3*, 256–260.
26. Hill, H. D.; Millstone, J. E.; Banholzer, M. J.; Mirkin, C. A. The Role Radius of Curvature Plays in Thiolated Oligonucleotide Loading on Gold Nanoparticles. *ACS Nano* **2009**, *3*, 418–424.
27. Yu, W. W.; Qu, L.; Guo, W.; Peng, X. Experimental Determination of the Extinction Coefficient of CdTe, CdSe, and CdS Nanocrystals. *Chem. Mater.* **2003**, *15*, 2854–2860.
28. Klimov, V. I.; McBranch, D. W. Femtosecond 1p-to-1s Electron Relaxation in Strongly Confined Semiconductor Nanocrystals. *Phys. Rev. Lett.* **1998**, *80*, 4028–4031.

29. Norris, D. J.; Bawendi, M. G. Measurement and Assignment of the Size-Dependent Optical Spectrum in CdSe Quantum Dots. *Phys. Rev. B* **1996**, *53*, 16338–16346.
30. Bullen, C.; Mulvaney, P. The Effects of Chemisorption on the Luminescence of CdSe Quantum Dots. *Langmuir* **2006**, *22*, 3007–3013.
31. Munro, A. M.; Jen-La Plante, I.; Ng, M. S.; Ginger, D. S. Quantitative Study of the Effects of Surface Ligand Concentration on CdSe Nanocrystal Photoluminescence. *J. Phys. Chem. C* **2007**, *111*, 6220–6227.
32. Knowles, K. E.; Tice, D. B.; McArthur, E. A.; Solomon, G. C.; Weiss, E. A. Chemical Control of the Photoluminescence of CdSe Quantum Dot−Organic Complexes with a Series of Para-Substituted Aniline Ligands. *J. Am. Chem. Soc.* **2009**, *132*, 1041–1050.
33. Morris-Cohen, A. J.; Vasilenko, V.; Amin, V. A.; Reuter, M. G.; Weiss, E. A. Model for Adsorption of Ligands to Colloidal Quantum Dots with Concentration-Dependent Surface Structure. *ACS Nano* **2011**, *6*, 557–565.
34. Peterson, M. D.; Jensen, S. C.; Weinberg, D. J.; Weiss, E. A. Mechanisms for Adsorption of Methyl Viologen on CdS Quantum Dots. *ACS Nano* **2014**, *8*, 2826–2837.
35. Peters, J. W.; Lanzilotta, W. N.; Lemon, B. J.; Seefeldt, L. C. X-Ray Crystal Structure of the Fe-Only Hydrogenase (CpI) from *Clostridium pasteurianum* to 1.8 Angstrom Resolution. *Science* **1998**, *282*, 1853–1858.
36. King, P. W.; Posewitz, M. C.; Ghirardi, M. L.; Seibert, M. Functional Studies of [FeFe] Hydrogenase Maturation in an *Escherichia coli* Biosynthetic System. *J. Bacteriol.* **2006**, *188*, 2163–2172.
37. Santangelo, J. D.; Dürre, P.; Woods, D. R. Characterization and Expression of the Hydrogenase-Encoding Gene from *Clostridium acetobutylicum* P262. *Microbiology* **1995**, *141*, 171–180.
38. Medintz, I. L.; Konnert, J. H.; Clapp, A. R.; Stanish, I.; Twigg, M. E.; Mattoussi, H.; Mauro, J. M.; Deschamps, J. R. A Fluorescence Resonance Energy Transfer-Derived Structure of a Quantum Dot-Protein Bioconjugate Nanoassembly. *Proc. Natl. Acad. Sci. U.S.A.* **2004**, *101*, 9612–9617.
39. Cui, S.-C.; Tachikawa, T.; Fujitsuka, M.; Majima, T. Photoinduced Electron Transfer in a Quantum Dot−Cucurbituril Supramolecular Complex. *J. Phys. Chem. C* **2011**, *115*, 1824–1830.
40. Robel, I.; Kuno, M.; Kamat, P. V. Size-Dependent Electron Injection from Excited CdSe Quantum Dots into TiO_2 Nanoparticles. *J. Am. Chem. Soc.* **2007**, *129*, 4136–4137.
41. Scholz, F.; Dworak, L.; Matylitsky, V. V.; Wachtveitl, J. Ultrafast Electron Transfer from Photoexcited CdSe Quantum Dots to Methyl Viologen. *ChemPhysChem* **2011**, *12*, 2255–2259.
42. Tvrdy, K.; Frantsuzov, P. A.; Kamat, P. V. Photoinduced Electron Transfer from Semiconductor Quantum Dots to Metal Oxide Nanoparticles. *Proc. Natl. Acad. Sci. U.S.A.* **2011**, *108*, 29–34.
43. Page, C. C.; Moser, C. C.; Chen, X.; Dutton, P. L. Natural Engineering Principles of Electron Tunnelling in Biological Oxidation−Reduction. *Nature* **1999**, *402*, 47–52.
44. Moser, C. C.; Keske, J. M.; Warncke, K.; Farid, R. S.; Dutton, P. L. Nature of Biological Electron Transfer. *Nature* **1992**, *355*, 796–802.
45. Scholes, G. D.; Jones, M.; Kumar, S. Energetics of Photoinduced Electron-Transfer Reactions Decided by Quantum Confinement. *J. Phys. Chem. C* **2007**, *111*, 13777–13785.
46. Saouma, C. T.; Pinney, M. M.; Mayer, J. M. Electron Transfer and Proton-Coupled Electron Transfer Reactivity and Self-Exchange of Synthetic [2Fe−2S] Complexes: Models for Rieske and mitoNEET Clusters. *Inorg. Chem.* **2014**, *53*, 3153–3161.
47. Bak, D. W.; Zuris, J. A.; Paddock, M. L.; Jennings, P. A.; Elliott, S. J. Redox Characterization of the FeS Protein mitoNEET and Impact of Thiazolidinedione Drug Binding. *Biochemistry* **2009**, *48*, 10193–10195.
48. Zuris, J. A.; Halim, D. A.; Conlan, A. R.; Abresch, E. C.; Nechushtai, R.; Paddock, M. L.; Jennings, P. A. Engineering the Redox Potential over a Wide Range within a New Class of FeS Proteins. *J. Am. Chem. Soc.* **2010**, *132*, 13120–13122.
49. Magalon, A.; Asso, M.; Guigliarelli, B.; Rothery, R. A.; Bertrand, P.; Giordano, G.; Blasco, F. Molybdenum Cofactor Properties and [Fe-S] Cluster Coordination in *Escherichia coli* Nitrate Reductase A: Investigation by Site-Directed Mutagenesis of the Conserved His-50 Residue in the NarG Subunit. *Biochemistry* **1998**, *37*, 7363–7370.
50. Dementin, S.; Belle, V.; Bertrand, P.; Guigliarelli, B.; Adryanczyk-Perrier, G.; De Lacey, A. L.; Fernandez, V. M.; Rousset, M.; Léger, C. Changing the Ligation of the Distal [4Fe4S] Cluster in NiFe Hydrogenase Impairs Inter- and Intramolecular Electron Transfers. *J. Am. Chem. Soc.* **2006**, *128*, 5209–5218.
51. Weinberg, D. R.; Gagliardi, C. J.; Hull, J. F.; Murphy, C. F.; Kent, C. A.; Westlake, B. C.; Paul, A.; Ess, D. H.; McCafferty, D. G.; Meyer, T. J. Proton-Coupled Electron Transfer. *Chem. Rev.* **2012**, *112*, 4016–4093.
52. Mayer, J. M. Proton-Coupled Electron Transfer: A Reaction Chemist's View. *Annu. Rev. Phys. Chem.* **2004**, *55*, 363–390.
53. Solis, B. H.; Hammes-Schiffer, S. Proton-Coupled Electron Transfer in Molecular Electrocatalysis: Theoretical Methods and Design Principles. *Inorg. Chem.* **2014**, *53*, 6427–6443.
54. Madden, C.; Vaughn, M. D.; Díez-Pérez, I.; Brown, K. A.; King, P. W.; Gust, D.; Moore, A. L.; Moore, T. A. Catalytic Turnover of [FeFe]-Hydrogenase Based on Single-Molecule Imaging. *J. Am. Chem. Soc.* **2011**, *134*, 1577–1582.
55. Zhao, J.; Holmes, M. A.; Osterloh, F. E. Quantum Confinement Controls Photocatalysis: A Free Energy Analysis for Photocatalytic Proton Reduction at CdSe Nanocrystals. *ACS Nano* **2013**, *7*, 4316–4325.